International Journal of Applied Earth Observation and Geoinformation 122 (2023) 103426

Contents lists available at ScienceDirect

International Journal of Applied Earth Observation and Geoinformation

journal homepage: www.elsevier.com/locate/jag

Methodology for measuring dendrometric parameters in a mediterranean forest with UAVs flying inside forest

Roberto Greco [a], Emanuele Barca [b,*], Pasi Raumonen [c], Manuela Persia [a], Patrizia Tartarino [a]

[a] Department of Soil, Plant and Food Sciences, University of Bari A. Moro, Via Amendola 165/A, 70126 Bari, Italy
[b] Water Research Institute, IRSA-CNR, Viale F. De Blasio 5, Bari 70132, Italy
[c] Computing Sciences, Tampere University, Korkeakoulunkatu 7, 33720 Tampere, Finland

ARTICLE INFO

Keywords:
UAV
Terrestrial structure from motion photogrammetry
Terrestrial laser scanner
Dendrometric parameters
Accuracy analysis
Pix4D

ABSTRACT

Accurate field measurements of tree morphological features are essential for effective forest inventory and the sustainable management of forest resources. Traditional methods involve time-consuming and expensive tree-by-tree measurements conducted by specialized technicians, which can lead to subjective measurement errors. To address these limitations, advanced sensor technologies have garnered attention in recent years. Terrestrial laser scanning (TLS) has been widely employed due to its high precision in deriving tree attributes at the plot level. However, TLS has certain drawbacks, including high acquisition costs, limited portability, and the requirement for specialized software and expertise. As alternatives, aerial photogrammetry and computer vision algorithms have emerged to obtain high-resolution 3D measurements of forest vegetation.

This study proposes a novel approach utilizing a small drone under the forest canopy to estimate biometric parameters such as trunk diameter at various heights and circumference. By joining the capabilities of drones with the structure-from-motion approach, this study presents a promising solution for cost-effective and accurate estimation of biometric parameters in forest inventories. Moreover, the results demonstrate superior accuracy compared to those reported in previous studies with improvements up to one order of magnitude.

1. Introduction

1.1. Monitoring forest characteristics: classic management practices

Field measurements of trees' primary morphological features play a key role in acquiring an effective forest inventory and formulating sustainable strategies for the utilization of forest resources. Monitoring these features enables us to grasp the characteristics of the forest ecosystem and implement appropriate management practices that align with the specific environmental conditions. Forest resource knowledge follows a hierarchical structure (Luoma et al., 2017), where individual tree attributes are aggregated at the plot level, and subsequently, plot-level estimates are employed to derive comprehensive assessments of forest resources at the stand or large-area level. However, conducting surveys to gather dendrometric parameters (biometric parameters) is generally a resource-intensive and time-consuming effort due to the involvement of several specialized technicians (Holopainen and Talvitie, 2012).

To provide to diverse objectives, scales, available resources, and desired accuracy levels, various forest inventory techniques can be applied (Liang et al., 2016). The different inventory methods include point sampling and fixed plot sampling. These methods are applied based on specific situations, considering the inventory objectives. The selected method should be suitable for the geographic location and stand condition, as well as efficient in terms of the information gathered within a given time frame (Inventory Methods…, 2018). Typically, during forest surveys, tree information is collected through meticulous tree-by-tree measurements utilizing mechanical or optical instruments like callipers, hypsometers, and measuring tapes. The most commonly measured tree attributes in the field encompass tree species, stem diameter at breast height (DBH), and tree height (Luoma et al., 2017). Despite being prone to subjective measurement errors (Holopainen and Talvitie, 2012), field measurements remain at present the predominant method employed for collecting forest data (Ozkan and Demirel, 2018).

* Corresponding author.
E-mail address: emanuele.barca@ba.irsa.cnr.it (E. Barca).

https://doi.org/10.1016/j.jag.2023.103426
Received 12 April 2023; Received in revised form 23 June 2023; Accepted 13 July 2023
Available online 17 July 2023

1.2. Enhanced management practices for measurements of tree morphology

In recent years, there has been a growing interest among forest managers and researchers in exploring alternative methods (Piermattei et al., 2019) for deriving tree attributes, particularly through the utilization of remote sensing technologies and approaches. The integration of remotely sensed (RS) data in forestry is driven by the objective of enhancing cost efficiency, precision, and timeliness in forest information (Mcroberts and Tomppo, 2007; White et al., 2016; Iglhaut et al., 2019; Gao et al., 2020; Brede et al., 2019; Brede et al., 2022).

Terrestrial laser scanning (TLS) currently stands as the most accurate method for generating point clouds at the plot level and deriving various tree attributes, including trunk circumference, tree density, tree positions, diameter at breast height (DBH), volume, and stem curves. Introduced in the early 2000 s, TLS has experienced significant advancements in sensor and algorithm development, enabling the explicit assessment of in-situ 3D forest structure and revolutionizing the monitoring and quantification of ecosystem structure and function (Calders et al., 2020). The key advantage of TLS in forest inventories lies in its capacity to rapidly and automatically document the forest with millimeter-level detail (Liang et al., 2016). However, drawbacks of this technology (Piermattei et al., 2019) include high acquisition costs, limited portability (except for lightweight systems), and the necessity of expertise in processing scanner data with specialized software. Furthermore, TLS incurs additional costs related to equipment (both field and lab) and time required for deployment and data processing (White et al., 2016).

More recently, considerable attention has been given to the utilization of structure-from-motion (SfM) and computer vision algorithms for acquiring high spatial resolution three-dimensional (3D) measurements of forestry vegetation. SfM is a passive technique that generates 3D point clouds from sequences of overlapping 2D images captured by digital still cameras (Iglhaut et al., 2019). These 3D point clouds can be employed in forest studies for 3D modelling of trees, utilizing other techniques as presented in this paper. The initial applications of SfM in vegetation structure studies can be traced back approximately ten years ago, involving the use of aerial imagery obtained through a kite aerial photography rig (KAP) system (Dandois and Ellis, 2010; Dandois and Ellis, 2013). Subsequently, the emergence of unmanned aerial vehicles (UAVs) coupled with UAV flight planning applications facilitated the development of protocols applicable across diverse environments and conditions (Tmušić et al., 2020), thereby enabling the joint application of drones and SfM (aerial photogrammetry) in various settings, including forests for small-scale inventorying (Puliti et al., 2015).

While aerial photogrammetry by drones is limited to the reconstruction of visible surfaces in the image data, providing ground information only in areas with significant vegetation gaps (Iglhaut et al., 2019), the results obtained from UAV-SfM approaches differ according to forest types as they mainly detect the dominant tree layer, with smaller and overshadowed trees remaining largely undetected (Iglhaut et al., 2019). The limitations of traditional field data collection, the need for cost reduction in alternative to laser scanning solutions, and constraints associated with aerial photogrammetry have encouraged the application of terrestrial photogrammetry for forest inventory using low-cost data collection equipment such as handheld or pole/tripod-mounted cameras or smartphones (Marzulli et al., 2020).

1.3. The methodological proposal

The present study introduces a novel approach that utilizes a small drone to operate within forested areas beneath the forest canopy. This approach implements terrestrial structure-from-motion (SfM) techniques to estimate biometric parameters, focusing specifically on trunk diameter at various heights and circumference. To evaluate the impact of different camera settings on biometric estimation, a rigorous statistical analysis was conducted. The experimental setup has resemblance to the use of drones in indoor environments, which are characterized by partially enclosed spaces with limited flight space compared to most outdoor settings. Indoor environments often exhibit narrow and cluttered conditions with numerous obstacles (De Croon and De Wagter, 2018). Similarly, when manoeuvring through forests at the plot level, a comparable situation arises in outdoor scenarios. The results after methodology application demonstrate superior accuracy compared to those reported in previous studies with improvements up to one order of magnitude. The experimental plot is located at the Mercadante Forest located in the Apulia Region, southern Italy.

2. Material and methods

2.1. Research plot and field measurements

The forest plot used in our study is in the Apulia region of southern Italy. It is part of the Mercadante Forest (1300 ha) in Alta Murgia National Park (Fig. 1). The forest was created by hydrogeological afforestation work to counteract the descent of rainwater from the Murgia uplands after floods that struck the Bari city area in the early 1900 s. The plot is characterized by an even-aged forest stand, and the main tree species are Aleppo pine (*Pinus halepensis Miller*) and cypress (*Cupressus sempervirens L.*). The plot covers an area of 30 × 30 m and consists of 47 trees (~520 stems * ha^{-1}). All the trees in the plot were numbered, and the boundary of the area was identified with a yellow horizontal line on the trees near the perimeter.

Preliminary sampling was carried out to estimate the variance of the variables of interest.

By applying the Cochran formula with an error margin of 10%, the size (N) of the sample was assessed as 22 trees. Fig. 2a reports all the plot trees (green dots) and those selected after numbering and extraction randomly from an urn (red dots and circles).

On the trees of the reference sample, the sections orthogonal to the axis of the trunks at different heights were indicated with white tape (Fig. 2b): 1.30 m, 2.00 m, and 4.00 m from the ground. The heights of the sections were estimated along the axis of the trunk, starting from the ground and considering the direction indicated by the yellow and black tape (Fig. 2b).

For each tree in the sample, at the section at 1.30 m − 2.00 m − 4.00 m from the ground were measured:

- n. 2 orthogonal diameters (the first in the north–south direction and the second perpendicularly more or less) with callipers;
- circumference with the measuring tape.

The north orientation was also indicated with a vertical red line to make the trees identifiable in the three-dimensional reconstruction (point cloud). The detection position of the diameters of the sections was indicated with a vertical line of white tape where the calliper touched the trunk.

Within the area, 15 markers were placed on poles of varying height, from 80 to 160 cm. The markers were numbered on both faces, so that they could be identified in the images from all sides of the area and used as manual tie points (MTPs) during photogrammetric processing. MTPs are 3D points corresponding to a feature that is marked (clicked) by the user in the images. They can be used to assess and improve relative reconstruction accuracy (Support pix4D).

2.2. Photogrammetry data collection and description

The images were captured with a DJI Mavic Air drone piloted in manual mode, which flew under the canopy cover. The DJI GO 4 App was used during the survey phases. The dimensions of the drone were 168 × 184 × 64 mm; it had a weight of 430 gr and was equipped with a camera with a ½0.3′’ CMOS sensor, effective pixels, 12 MP, 35 mm

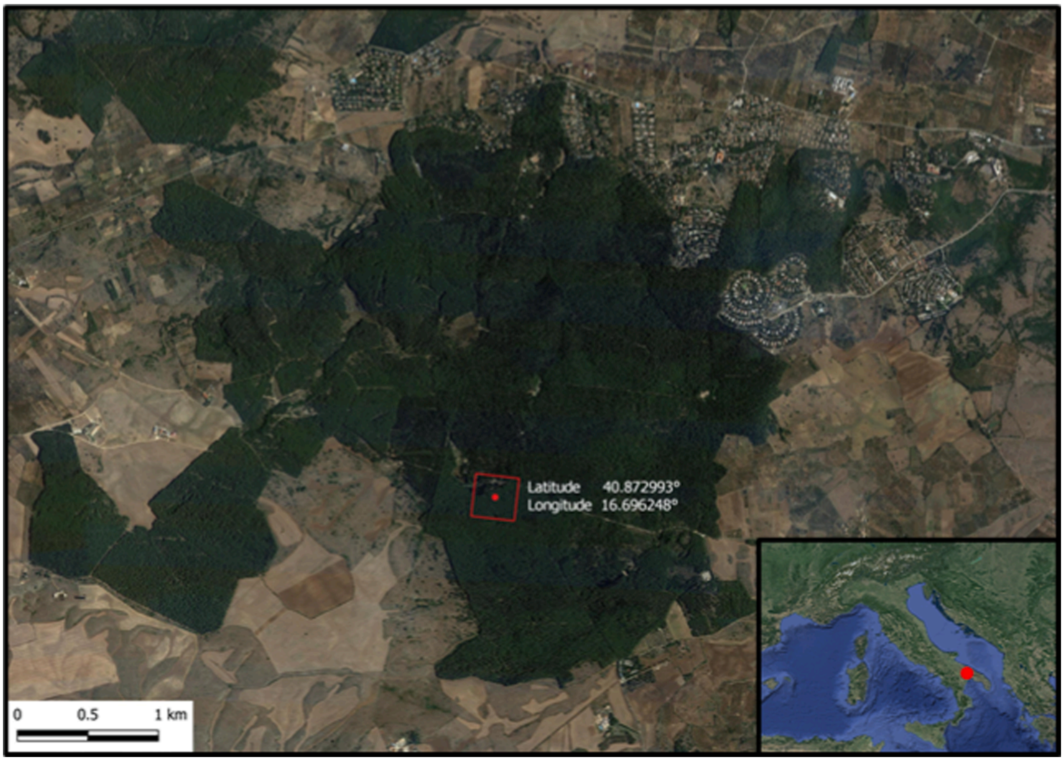

Fig. 1. The red point indicates the center of the study area (Latitude: 40.872993° - Longitude: 16.696248°). (For interpretation of the references to colour in this figure legend, the reader is referred to the web version of this article.)

(a) **(b)**

Fig. 2. The study plot. **(a)** Trees spatial distribution within study area. Red encircled points are trees belonging to the sample. **(b)** Reference section on the stem axes. (For interpretation of the references to colour in this figure legend, the reader is referred to the web version of this article.)

equivalent lens, 24 mm, and aperture f 2.8.

The camera was installed on a 3-axis gimbal. The photos were taken in "timed shot" mode, with shutter speed every 2 s, with "tripod mode" activated, to ensure an overlap between photos of at least 65%.

During image acquisition, the "enable visual obstacle avoidance" system was disabled. In all the surveys carried out, the drone trajectory was determined manually with the remote controller, following a path that was as straight as possible and avoided trees or low branches.

The images were acquired by carrying out five different surveys in "free flight or terrestrial mode" using three different settings (Table 1) related to the flight altitude and the inclination of the camera.

The survey types were, in summary, three outside the study area, approximately parallel to the plot boundary (Liang et al., 2014), and two

Table 1
Camera settings.

Setting	Camera tilt	Ground Distance [m]	Distance from plot boundary [m]
1	Upward (~20°)	0.5—1	0—0.5
2	Downward (~20-30°)	3—4	3—5
3	Downward (~20-30°)	4—7	3—5

Table 2
Number of captured images and data collection time.

Flight	Captured Images in each flight	Setting	Data collection time [min: sec]
1 - outside	277	3	11:03
2 - outside	280	2	10:48
3 - outside	292	1	10:46
4 - inside	197	3	7:56
5 - inside	216	1	8:21

inside the study area (Table 2 and Fig. 3). The purpose of the inside surveys was to obtain better accuracy of 3D reconstruction along the boundary.

Different flights were carried out with variable settings, with the aim of acquiring as many images as possible of the area to capture the tree details (the ground, stem, branches and canopy).

The images were captured in JPEG format (aspect ratio 4:3) with the camera settings in auto mode and geotagging enabled. Images were acquired at the highest resolution (4056 × 3040 pixels) with an ISO between 100 and 400 and with an exposure time varying between 1/15 and 1/30.

2.3. Photogrammetry point cloud processing workflow

The commercial software Pix4Dmapper (Pix4Dmapper SA) based on the SfM algorithms was adopted to derive dense point clouds from the overlapping images. This software can process terrestrial images captured by a digital camera or aerial images taken by UAV. The SfM workflow can be found in (Ullman, 1979; Westoby et al., 2012; Micheletti et al., 2015). This processing workflow consists of four main steps: (1) initial camera orientation, (2) MTP identification in the images, (3) final camera orientation (bundle block adjustment), and (4) dense point cloud computation based on dense image matching (Piermattei et al., 2019). Detailed descriptions of the Pix4D workflow can be found in the study of Küng et al. (2011).

The photogrammetric processing for generating the point cloud involved organizing different combinations of available images and adjusting software parameters that are modifiable. A total of sixteen point clouds were generated, with the first eight derived from processing images captured during outside flights, while the remaining point clouds resulted from both inside and outside flights. Specifically, point clouds 1 to 4 were generated using images from three outside surveys (flights 1, 2, and 3 as indicated in Table 2), point clouds 5 to 8 were created using images from the first and second flights, point clouds 9 to 12 were produced using all five flights (three outside and two inside the study area), and point clouds 13 to 16 were generated using flights 1, 2, and 4.

In the study area, five MTPs (Master Control Points) were identified, with the number of marked images directly corresponding to the available image count. Software parameters were changed to assess their influence on the resulting point cloud densification. Image scale, which defines the scale of the images where 3D points are computed, was set to 1/2 and 1/4; point density, which defines the density of the densified point cloud, was set to *optimal* to obtain a 3D point computed for every [4/image scale] pixel and set to *low* to compute a 3D point for every [16/

Table 3
Different combination of flight and software parameters.

Point cloud	Flight	Number of flights	Captured images	Calibrated images	Image Scale	Point Density
1	Outside	3	849	759	1/2	Optimal
2	Outside	3	849	759	1/4	Optimal
3	Outside	3	849	759	1/2	Low
4	Outside	3	849	759	1/4	Low
5	Outside	2	557	487	1/2	Optimal
6	Outside	2	557	487	1/4	Optimal
7	Outside	2	557	487	1/2	Low
8	Outside	2	557	487	1/4	Low
9	Outside/ Inside	5	1262	1150	1/2	Optimal
10	Outside/ Inside	5	1262	1150	1/4	Optimal
11	Outside/ Inside	5	1262	1150	1/2	Low
12	Outside/ Inside	5	1262	1150	1/4	Low
13	Outside/ Inside	3	754	668	1/2	Optimal
14	Outside/ Inside	3	754	668	1/4	Optimal
15	Outside/ Inside	3	754	668	1/2	Low
16	Outside/ Inside	3	754	668	1/4	Low

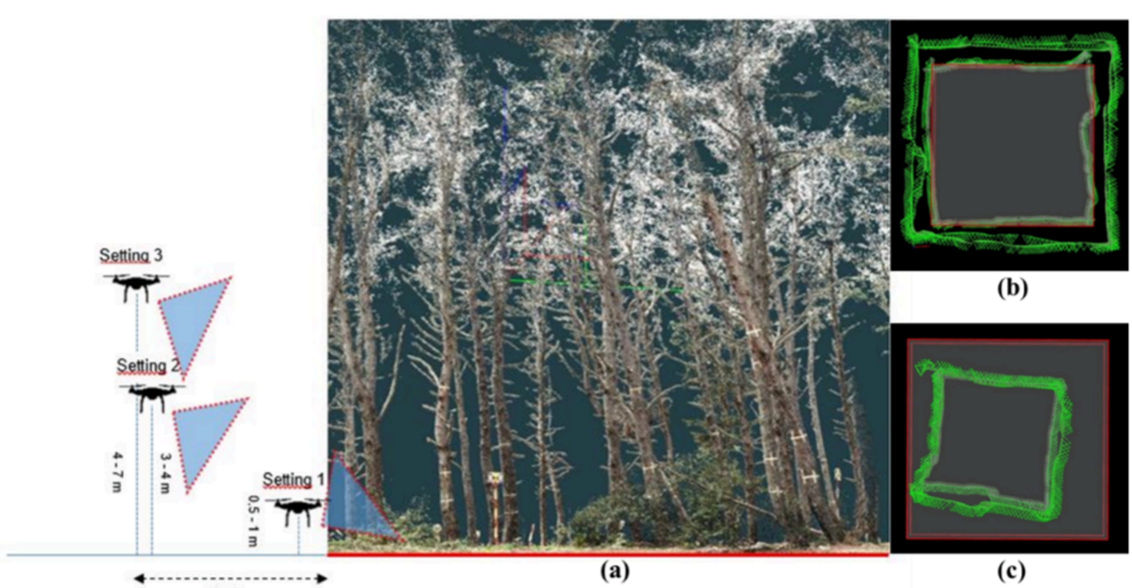

Fig. 3. Data collection. **(a)** Representation of the three settings used; **(b)** Outside surveys; **(c)** Inside surveys.

image scale] pixel (Marzulli et al., 2020). The different combinations of the flight and software parameters used are reported in Table 3. Data were processed using a 64-bit system with an Intel Core i7-8700 CPU at 3.2 GHz, and 32.0 GB RA, with version 4.6.4 of the Pix4DMapper software.

3. Statistical analysis and point cloud processing.

3.1. Sample size and scheme

The estimation of sample size is derived from the standard error formula of the population mean of the variable of interest and from the related confidence interval. After some manipulation, the Cochran formula (1977) can be obtained, allowing the computation of the sample size ń at a desired level of precision, given the estimated variability present in the population.

The formula is as follows:

$$n' = (z_{\alpha/2})^2 \sigma^2 / E^2 \quad (1)$$

where $z_{\alpha/2}$ is the quantile of the standard normal associated with the α level of significance, σ^2 is the estimated population variance, E is the acceptable margin error for the mean estimation (i.e., the size of the mean confidence interval). Then, by multiplying μ/μ (population mean) by the second member of the equality, the formula obtained is as follows:

$$n' = (z_{\alpha/2})^2 CV^2 / Efrac^2 \quad (2)$$

where CV is the coefficient of variation and Efrac is the error margin expressed as a fraction of the absolute error.

3.2. Accuracy analysis

To carry out the accuracy analysis on each point cloud, a set of error indices was applied. Willmott and Mastuura (2005) proposed a general form of the error index reported in Eq. (3). By changing the values of the α parameter, it is possible to derive an array of well-known error indices:

$$\bar{r}^{\alpha} = \left[\frac{\sum_{j=1}^{n} |r_j|^{\alpha}}{n}\right]^{\frac{1}{\alpha}} \quad (3)$$

- the Mean-Bias Error (MBE) (α = 1 and the sign of the residuals is not removed):

$$MBE = \frac{\sum_{i=1}^{n} r_i}{n} \quad (4)$$

- the Root Mean Square Error (RMSE) (α = 2):

$$RMSE = \sqrt{\frac{\sum_{i=1}^{n} (r_i)^2}{n}} \quad (5)$$

The formula in Eq. (4) is not only a trivial estimation of the residuals' distribution average but also conveys useful information about the bias in the model's predictions (Chai and Draxler, 2014). In fact, an approximately null value of MBE indicates a good balance between underestimation and overestimation. Generally, it is difficult to assign a qualitative degree (excellent, good or poor) to the goodness of fit since error indices generally lack a superior limit, this problem can be overcome by means the Mean Absolute Percentage Error (MAPE):

$$MAPE = \frac{1}{n}\sum_{i=1}^{n}\frac{|z^*(x_i) - z(x_i)|}{z(x_i)} = \frac{1}{n}\sum_{i=1}^{n}\frac{|r_i|}{z(x_i)} = \frac{1}{n}\sum_{i=1}^{n}\frac{r_i^a}{z(x_i)} \quad (6)$$

MAPE index is dimensionless since any residual is rescaled in terms of the corresponding observed value. Since it is an average relative value, it is possible to define thresholds of goodness of fit; for example, if MAPE is less than 0.1 (or 10% if it is expressed as a percentage), this can be considered a good result according to the Lewis scale (Lawrence and Klimberg, 2016; Barca et al., 2017). The R library used for using the error metrics mentioned above was {Metrics}.

3.3. Precision analysis

The precision analysis was carried out by means of Pearson's linear correlation coefficient (Barca et al., 2017). It is a bivariate parametric index that quantifies the strength of the (linear) relationship between pairs of variables. In this study, it was applied to assess the relationship between the in-field measurements and values computed from the point cloud. Given two samples X and Y having the same size N, the sample Pearson's correlation is determined using the following formula:

$$r_{xy} = \frac{\sum_{i=1}^{N}(x_i - \bar{x})(y_i - \bar{y})}{\sqrt{\sum_{i=1}^{N}(x_i - \bar{x})^2}\sqrt{\sum_{i=1}^{N}(y_i - \bar{y})^2}} \quad (7)$$

where x_i and y_i are two generic elements of samples X and Y, respectively. Finally, $\bar{x}$ and $\bar{y}$ are the means of samples X and Y, respectively. The numerical results are constrained in the interval (-1, 1). The interpretation of the correlation index outcomes is the following: at 1, the correlation is maximal, at 0 it is null and at −1 the inverse correlation is maximal.

3.4. Point cloud processing

3.4.1. Point height estimation

Before the identification and modelling of the tree stems, the point cloud produced by photogrammetry was filtered to remove nontree points, such as points from the ground and noise. First, the point cloud was clipped to the area of interest to exclude areas outside the plot. Afterwards, the points cloud P was geometrically described as a subset of R^3, namely the 3d space.

To determine the ground level, the point cloud was partitioned so that, horizontally, it consisted of squares with a side length of 0.5 m. Let us consider a particular point defined as $(x\_min, y\_min, z\_min) = minimum(P)$ as the point with the minimum x, y, z-coordinates of the points in P. Each subset $S_{i,j}$ of the partition is uniquely identified by a pair of indices (i, j) of the points that bounds the subset to a specific square of 0.5 m side length. By ignoring the third coordinate (z), it is possible to construct partitions of the points cloud defined as:

$$(i,j) = floor\left(\frac{(x,y) - (x_{min}, y_{min})}{0.5}\right) + 1, \quad (8)$$

where floor denotes the rounding down to the closest integer. Let us consider for each $S_{i,j}$ the related $z_{min\_i\_j}$ as the minimum elevation, so for each $S_{i,j}$ it is possible to define two further subsets:

$$B_{i,j} = \{(x,y,z) \in S_{i,j} | z < z_{min\_i\_j} + 0.3\} \quad (9)$$

$$G_{i,j} = \{(x,y,z) \in B_{i,j} | z < z_{10}\} \quad (10)$$

z_{10} = 10th percentile of the z − coordinate in each $B_{i,j}$

From each $G_{i,j}$, by averaging all its elements, it is possible to define a special point called $vertex = (mean(x), mean(y), mean(z))$. Let us now consider V as the set of all the vertices; if only the first two coordinates are considered, the set V is planar, and Delaunay triangulation can be applied (Dwyer, 1987). By adding back the z-coordinate to the vertices of triangles, the triangulation becomes a continuous surface in R^3, namely the 3-d space, which represents an approximation of the ground level. In this way, it becomes possible to measure the height of each point of the cloud by projecting it on the surface. On the surface, the projected point assumes coordinates (x, y, z_0), and consequently, the actual point height is z - z_0.

3.4.2. Tree isolation.

Tree isolation is a very complex task consisting of multiple passages, as summarized in the following sections.

- *Clustering points (defining patches)*

First, the filtered point clouds are segmented according to the common forest topology. The procedure proceeds by segmenting the point cloud into trees and then into branches by considering the smallest meaningful units (called patches) on the tree surface. The diameter of the patches varies between 6 and 12 cm. The patch centres form the nodes, and the connections between the neighbours are the edges of the patch graph (Raumonen et al., 2015).

- *Locating stems*

The stems are individuated as large clusters of patches called components. The connected components of the patches are determined between 2 and 3 m from the ground, and only components with at least 25 patches are selected. These subsets of the point cloud can be considered sections of the stems (Fig. 4). They are bases for the next step of the process wherein the shortest paths are computed from every patch to a patch in some base. Coloured stem sections represent the components between 2 and 3 m.

- *Shortest paths*

The shortest paths are computed by means of Dijkstra's algorithm (Fredman and Tarjan, 1987), where the graph's nodes are the seed points of the patches and the edges are defined by the neighbours of the patches. The original algorithm was modified to manage the case of gaps in the sequence of the nodes (incomplete graph). The algorithm is iterative, and each iteration has restrictions on how long the paths can be relative to the height of the node. In this way, the paths can be limited horizontally, and gaps can be located to bridge them with new edges in the graph.

- *Defining trees*

Trees are defined as those patches whose shortest path ends at the same stem section. To complete the trees, since the base is a section between 2 and 3 m above the ground, the shortest paths are determined from the base towards the ground. Patches whose path length is a maximum of 1.1 larger than the height of its base are selected.

- *Defining stems*

Each tree is segmented into stems and branches using a modified version of the method presented in Raumonen et al. 2015. In this method, the base of the tree is defined as the bottom 50 cm of its point cloud. The branching points are located topologically by a small collection of patches that form a short section of the tree and move one layer of patches at the time forwards from the base to the stem and branches. If the patch collection becomes disconnected as it moves through two or more forks, a branching point is detected. The number of shortest paths going through each fork then determines which fork continues the stem and which is a branch. This results in stems that are now separated from their branches. The stem part is used for the geometric modelling.

- *Geometric modelling of stems*

Each isolated stem, which is also measured in the field, is modelled following different approaches to estimate its diameters, circumferences and volume up at given different heights. First, cylinders are fitted for the whole segmented stem to measure the volumes up to given heights (1.3, 2.0, 4.0 and 8.0 m). The cylinder is fitted from the base on, and next, other cylinders are fitted until the whole stem is modelled (Fig. 5).

For each cylinder, multiple different lengths are first fitted, and the cylinder with the highest *surface coverage* is selected. The surface coverage measures how much of the cylinder is covered with points and thus measures how reliable the fit is (Marzulli et al. 2020). Moreover, each cylinder is fitted to a longer section than it is intended to cover in the stem so that the axis direction is less sensitive to local noise and point cloud gaps. The centre section is weighted more than the top and bottom sections to obtain a better radius estimate. Next, for certain heights of

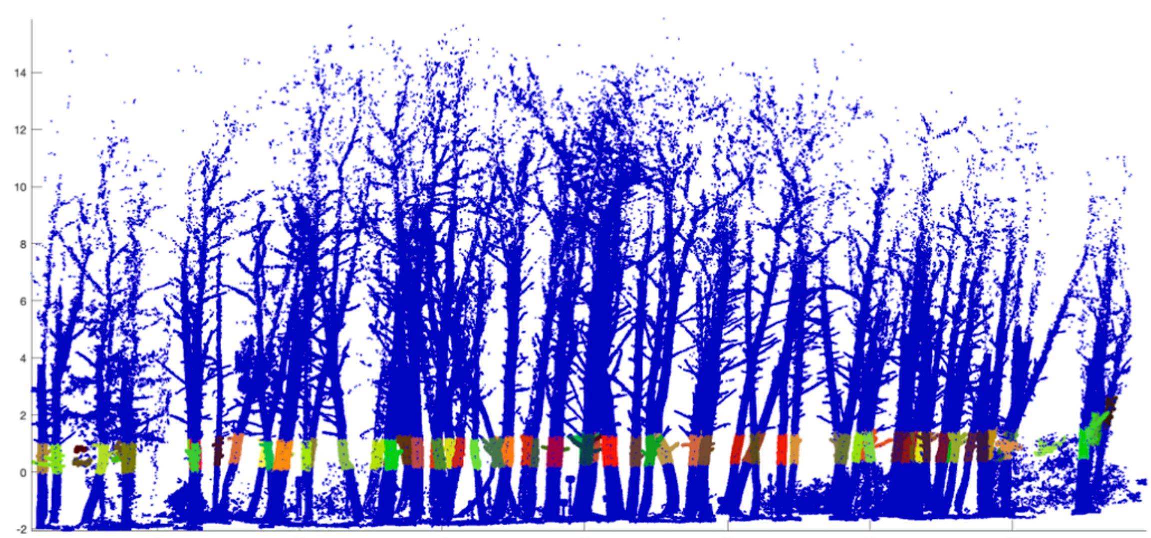

Fig. 4. Locating stems from the point cloud. Each coloured section is a collection of at least 25 patches between 2 and 3 m above the ground and they form stem sections.

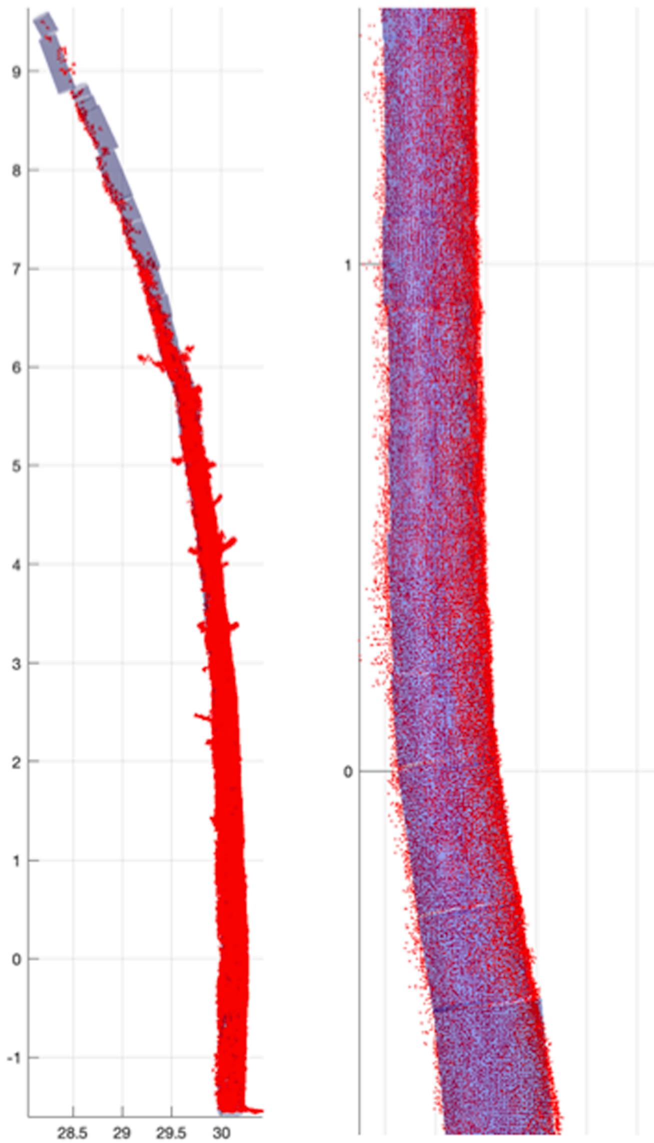

Fig. 5. Examples of the cylindrical stem models.

the stem (1.3, 2.0, 4.0 and 8.0 m) where field measurements are available, diameters and circumference are modelled with cylinders and *sector approximations*. First, the correct location is approximately found from the point cloud using the first cylinder model of the stem. The in-field measurements are fixed by putting marker tape on the stem corresponding to the given heights. Then, the marker tape is recognized based on the intensity values of the points to match the diameter and circumference estimates from the point cloud and the field measurements. An approximately 80 cm section of the stem is selected around the correct height for the final cylinder parameter estimation. However, the points are weighted so that the highest weight value is one at the target height (marker tape location), and the weight decreases towards the ends of the long section to zero. Next, the south-north and west-east diameters and the circumference are measured using the *sector model*. A 10 cm (or 15 or 20 cm if points are not sufficient) section around the target height is selected using the fitted cylinder, and the points are projected into the plane orthogonal to the cylinder axis. Then, the plane points are partitioned into 36 sectors of 10°each. For each sector, a "sector point" is formed by computing the average of the points in the sector. If there are empty sectors, their points are interpolated. The south-north and west-east diameters are then the distances between certain sector points. The circumference is the sum of the distances between the adjacent sector points.

4. Results

4.1. Point cloud generation

Different combinations of captured images and software parameters (image scale and point density) involved different elaboration times and variable average point cloud densities, as shown in Table 4.

Table 4 shows that point clouds 8 and 16 were generated with shorter times and by low average point cloud density.

4.2. Check for height effect on predictions

As already reported, the in-field measurements of diameters and circumferences refer to three different heights (1.3, 2.0, 4.0 and 8.0 m). An analysis to check the independence of diameter predictions from heights was performed as follows. MAPE[%] diameter errors were split into three groups to check if the different heights adversely impacted diameter predictions. The Shapiro-Wilk test of normality was conducted on the three groups with the following results (Table 5):

All the groups were non-Gaussian; therefore, we applied nonparametric tests next. The nonparametric Levene test for homogeneity of was performed on the three groups with the following results: test statistic = 0.98, p value = 0.39 (homoscedastic). Finally, the Kruskal-Wallis nonparametric ANOVA test was applied to the three groups with the following results: Kruskal-Wallis chi-squared = 0.67, df = 2, p value = 0.72 (same averages). Fig. 6a shows the outcome of the nonparametric ANOVA test; in fact, the average values (black horizontal lines within the grey boxes in Fig. 6a) were approximately aligned horizontally. Therefore, the point clouds were demonstrated to be good enough to guarantee a diameter prediction error independent of the measurement heights. The same kind of analysis was carried out to check the independence of circumference predictions from heights. MAPE[%] diameter errors were split once more into three groups corresponding to the groups of measurements carried out at each considered height.

The Shapiro-Wilk test of normality was applied to the three groups with the following results (Table 6):

All the groups were non-Gaussian; therefore, we used nonparametric

Table 4
Processing time and average point cloud density.

Point cloud	Flight	Processing time (point cloud densification)	Average Point cloud Density [points/m^3]
1	Outside	2 h 31′	24.465
2	Outside	46′	10.414
3	Outside	52′	11.077
4	Outside	21′	5.433
5	Outside	1 h 17′	28.578
6	Outside	24′	11.874
7	Outside	28′	12.451
8	Outside	11′	5.793
9	Outside/ Inside	7 h 03′	41.134
10	Outside/ Inside	2 h 06′	16.688
11	Outside/ Inside	2 h 29′	17.388
12	Outside/ Inside	52′	8.125
13	Outside/ Inside	3 h 09′	43.834
14	Outside/ Inside	59′	17.028
15	Outside/ Inside	1 h 05′	17.502
16	Outside/ Inside	23′	7.675

Table 5
Outcomes of Gaussianity tests on the three groups for each height.

Group	Statistic W	p-value	Outcome
A	0.60	1.834e-05	nogaus
B	0.72	0.0002839	nogaus
C	0.66	5.699e-05	nogaus

tests in the next step. The nonparametric Levene test for homogeneity of variance was performed on the three groups with the following results: test statistic = 0.19, p value = 0.83 (homoscedastic). Finally, the Kruskal-Wallis nonparametric ANOVA test was applied to the three groups with the following results: Kruskal-Wallis chi-squared = 0.0045, df = 2, p value = 0.9978 (same averages). Fig. 6b shows the outcomes of the nonparametric ANOVA test; in fact, the average values (black horizontal lines within the grey boxes in Fig. 6b) are approximately aligned horizontally. Therefore, the point clouds were demonstrated to be good enough in terms of size and accuracy to guarantee a circumference prediction error independent of the measurement heights.

4.3. Check for internal/external flight effect on predictions

The drone flights can be categorized into two groups: those that crossed the forest and those that rotated around it. Determining if these two kinds of flights influenced the accuracy of the predictions for circumferences and diameters differently was of interest. For this particular problem, MAPE[%] accuracy values of circumferences was split into two groups (external vs. internal flights). Then, the Shapiro-Wilk test of normality was conducted on the three groups with the following results (Table 7):

All the groups were non-Gaussian; therefore, we used nonparametric tests in the next step. The nonparametric Levene test for homogeneity of variance was performed on the three groups with the following results: test statistic = 0.41, p value = 0.54 (homoscedastic). Finally, the Kruskal-Wallis nonparametric ANOVA test was applied to the three groups with the following results: Kruskal-Wallis chi-squared = 0.099, df = 1, p value = 0.75 (same averages) (Fig. 7a and 7b).

All the groups were non-Gaussian; therefore, we used nonparametric tests in the next step. The nonparametric Levene test for homogeneity of variance was performed on the three groups with the following results: test statistic = 0.40, p value = 0.54 (homoscedastic). Finally, the Kruskal-Wallis nonparametric ANOVA test was applied to the three groups with the following results: Kruskal-Wallis chi-squared = 0.099, df = 1, p value = 0.75 (same averages) (Fig. 7a and 7b).

The same analysis was repeated for diameter MAPE[%] errors. The Shapiro-Wilk test of normality was computed on the three groups with the following results (Table 8):

All the groups resulted non-Gaussian; therefore, next tests have to be non-parametric to be effective. The non-parametric Levene test for variance homogeneity has been performed on the three groups with the following results: Test Statistic = 0.40, p-value = 0.54 (homoscedastic). Finally, the Kruskal-Wallis non-parametric ANOVA test has been applied to the three groups with the following results: Kruskal-Wallis chi-squared = 0.099, df = 1, p-value = 0.75 (same averages).

Once more, no significant effect was found due to the different kinds of flight on predictions of diameters and circumferences.

4.4. Accuracy analysis

In the given tree sampling, in-field measurements of diameters and circumferences were available; therefore, after the stem reconstruction described above, it is possible to assess the departures (errors) between observations and reconstructed values (Tables 9 - 10).

In Table 9, approximately 81% of the point clouds have an average MAPE[%] of less than 10%.

Table 10 shows that approximately 88% of the point clouds have an average MAPE[%] of less than 10%.

Based on those results, we concluded that the reconstruction of the diameters and circumferences of the samples was very accurate, apart from those of point clouds #8 and #16 (marked in bold). Therefore, both datasets coming from flights and the reconstruction models worked very well.

4.5. Precision analysis

Once the accuracy of the predicted values of diameters and circumferences was established, the next step was to assess the precision of the reconstructions by evaluating the Pearson's correlation index between observations and reconstructed values from the point clouds (Table 8). Table 11 shows that 9 point clouds out of 16 reached 98% of the correlation maximum score, and only 2 point clouds (#8 and #16) were invalid (i.e., did not provide valid tree parameter estimations of diameter and circumference). The results obtained proved that repeating the assessment on the same trees with different parameters of the camera and SfM, they converge approximately to each other.

Table 6
Outcomes of Gaussianity tests on the three groups for each height.

Group	Statistic W	p-value	Outcome
A	0.64	4.43e-05	nogaus
B	0.73	0.00039	nogaus
C	0.74	0.00052	nogaus

Table 7
Outcomes of Gaussianity tests on the two groups for each kind of flight.

Group	Statistic W	p-value	Outcome
A	0.67	0.00091	nogaus
B	0.65	0.00065	nogaus

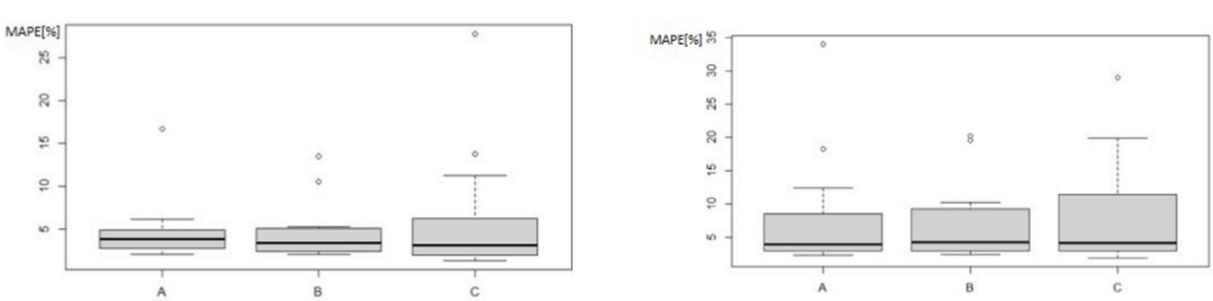

(a) (b)

Fig. 6. Comparisons of the three groups (by classes of height) of: **(a)** diameter's errors averages. **(b)** circumference's errors averages.

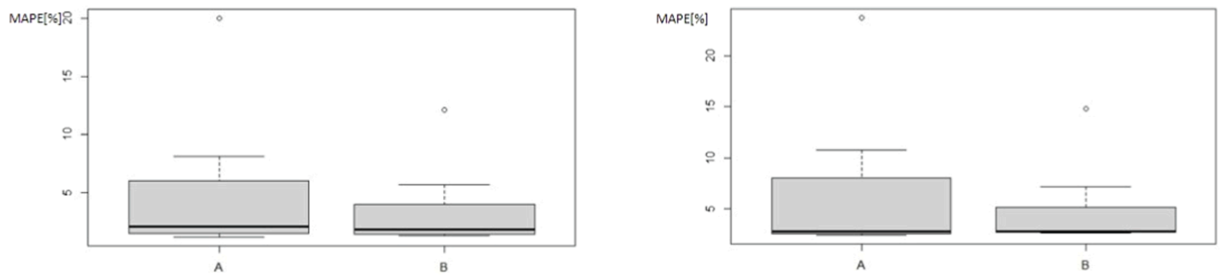

(a) **(b)**

Fig. 7. Comparison of the two groups (internal vs. external flights) of: **(a) c**ircumference's errors averages; (**b**) Diameter's errors averages.

Table 8
Outcomes of Gaussianity tests on the two groups for each kind of flight.

Group	Statistic W	p-value	Outcome
A	0.70	0.0023	nogaus
B	0.63	0.00037	nogaus

Table 9
Extraction Model diameter average errors-RMSE and MAPE[%]. Poor point clouds are marked in grey.

Point cloud index	Number of reconstructed trees	RMSE average [*cm*]	MAPE average [%]
1	22	1.05	2.44
2	21	0.92	2.57
3	21	0.96	2.79
4	11	4.06	10.79
5	22	0.89	2.59
6	21	2.23	5.26
7	20	0.99	2.77
8	**4**	**7.36**	**23.71**
9	22	0.92	2.69
10	22	0.96	2.87
11	22	0.92	2.73
12	18	2.75	7.20
13	22	0.92	2.66
14	21	1.02	3.07
15	22	0.88	2.63
16	**6**	**4.29**	**14.76**

Table 10
Extraction Model circumference average errors - RMSE and MAPE[%]. Poor point clouds are marked in grey.

Point cloud index	Number of reconstructed trees	RMSE average (cm)	MAPE average [%]
1	22	1.73	1.67
2	21	1.57	1.36
3	21	1.87	1.64
4	11	10.47	8.11
5	22	1.35	1.19
6	21	5.20	3.88
7	20	2.59	2.47
8	**4**	**19.92**	**20.03**
9	22	2.17	2.26
10	22	1.85	1.79
11	22	1.41	1.27
12	18	7.12	5.72
13	22	1.78	1.81
14	21	1.61	1.55
15	22	1.36	1.30
16	**6**	**10.94**	**12.15**

4.6. Assessment of similarity between point clouds

Sixteen point clouds were generated from different flights, and different parameters were provided to the SfM process. After the computations, the error size can be an effective indicator of the goodness of SfM parameter selection; therefore, analysing and comparing the error size between point clouds is a useful method for identifying the best parameter settings to gain the best point clouds. The *heatmap* can be a useful tool for performing that analysis and identifying similarities and differences between point clouds (Fig. 8). The numerical value considered is the MAPE[%] average attached to each cloud.

From visual inspection of the dendrogram, two main groups emerged: Cloud8 and Cloud16 and the remaining clouds. Cloud8 and Cloud16 were already identified from accuracy and precision analyses as the poorest clouds. The remaining clouds were further split into two groups: Cloud6, Cloud12 and Cloud4 from one side and the remaining clouds. Again, these three clouds were already identified as poor clouds based on the results of the previous analyses.

4.7. Basic statistics of point clouds

The analysis of the weighted average error indicated that the poorest point clouds were Cloud8, Clout16, and Cloud4 because the average exceeded the threshold of 10%. That threshold identifies optimal clouds, whereas the threshold of 5% identifies excellent clouds. Approximately 69% of the clouds had average errors lower than 5%: a very good overall result. However, comparing Tables 12 and 13, it appears that the diameter reconstruction had a lower accuracy than the circumference reconstruction. This is because diameters measured in the field are not parallel with the ground, but rather are inclined with respect to two orthogonal angles; this makes the assessment of the diameter more complex than that of the circumference. Consequently, the average errors of diameters were larger than those of circumferences.

In conclusion, based on the results in Tables 9, 10, 12 and 13, we identified the best point clouds according to the values of MAPE[%] and the number of actually reconstructed trees. Table 14 reports the best point clouds and the related parameters set in Pix4D Mapper software.

All point clouds in Table 14 had a value of MAPE average [%] (diameter average errors and circumference average errors) less than 5%, and they can be considered highly accurate according to the Lewis scale. In particular, point Cloud5, Cloud11 and Cloud15 (marked in bold) were the best based on the average MAPE[%] of diameter and circumference.

4.8. Better reconstructed trees

Since the tree reconstruction was implemented according to different point clouds coming from different flights and parameter tuning within the SfM computational process, an interesting advancement could be the individuation of the better reconstructed subzones of the study area. This check was accomplished by fixing a threshold of accuracy (MAPE

Table 11
The table reports the correlation coefficients between the in-field measurements and estimated values. Point clouds with lower correlation scores are shown in dark grey, while point clouds with the highest correlation scores are depicted in light grey. N-S columns represent the North-South diameters, and 2° columns refer to the orthogonal diameters relative to N-S.

	Diameter						Circumference		
Point Cloud	N-S	2°	N-S	2°	N-S	2°	1.30	2.00	4.00
1	0.98	0.97	0.98	0.96	0.97	0.97	0.99	0.99	1.00
2	0.98	0.98	0.99	0.96	0.96	0.96	1.00	0.99	0.98
3	0.98	0.97	0.98	0.95	0.98	0.95	0.99	0.98	0.98
4	0.95	0.75	0.89	0.96	0.60	0.93	0.90	0.96	0.69
5	0.97	0.96	0.97	0.96	0.97	0.97	0.99	0.99	1.00
6	0.87	0.83	0.86	0.84	0.85	0.75	0.90	0.86	0.85
7	0.98	0.96	0.96	0.94	0.97	0.96	0.97	0.98	0.98
8	0.00	0.00	0.00	0.00	0.00	0.00	0.00	0.00	0.00
9	0.97	0.97	0.98	0.97	0.96	0.97	1.00	0.99	0.99
10	0.97	0.97	0.97	0.95	0.96	0.98	0.99	0.99	0.99
11	0.98	0.97	0.98	0.96	0.95	0.97	1.00	1.00	0.99
12	0.88	0.81	0.89	0.75	0.79	0.92	0.87	0.83	0.85
13	0.96	0.97	0.97	0.97	0.97	0.96	0.99	0.99	1.00
14	0.97	0.98	0.97	0.95	0.96	0.98	0.99	0.99	0.99
15	0.97	0.97	0.97	0.97	0.96	0.97	0.99	0.99	0.99
16	0.00	0.00	0.00	0.00	0.00	0.00	0.00	0.00	0.00

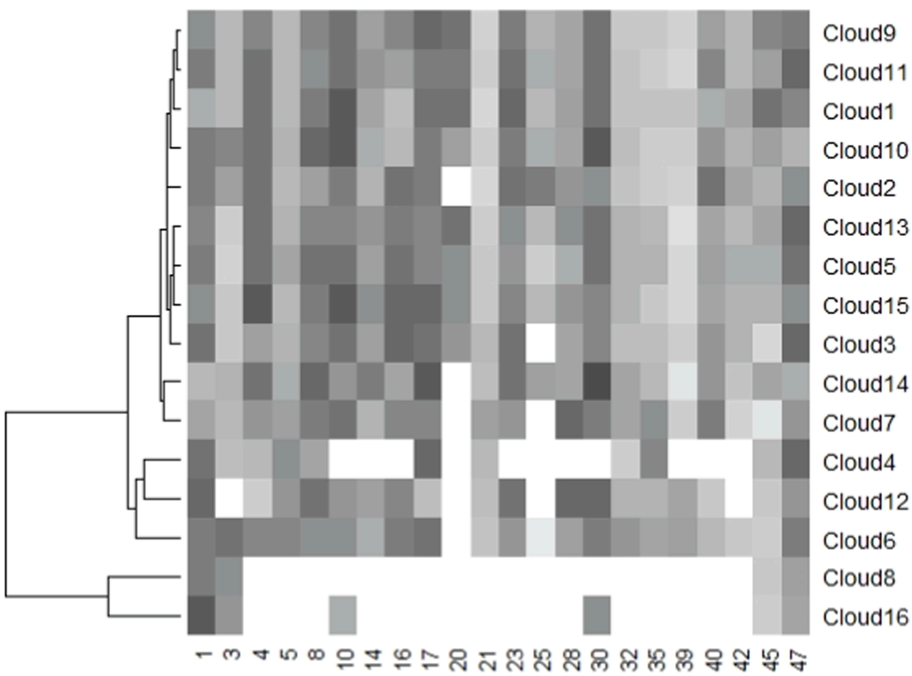

Fig. 8. Heatmap MAPE[%] levels at 1.3 m height.

[%]) and assessing the case frequency on which each tree has an accuracy lower than the considered threshold. The given threshold was 3.5%, which represents an accuracy level excellent. Fig. 9 shows a map with the sampled trees represented by a black dot identifying their positions inside the study area. The size of each dot is proportional to the frequency at which the tree's accuracy was better than 3.5%.

The map indicates that the northern part of the study area was characterized by excellent accuracy.

5. Discussion

The aim of the present study was to demonstrate the effectiveness of the use of a small drone to carry out undercover photogrammetric surveys in a forest environment, with the goal of quantifying parameters of dendrometric interest. This approach, in addition to simplifying the acquisition schemes, allows field operations to be carried out with times comparable or shorter than those based on the traditional terrestrial SfM survey, as reported in Piermattei et al. (2019), Liu et al. (2018) and Mokrosh et al. (2018).

Tables 3, 4, 9 and 10 highlight the main features that influence the quality of the results of the photogrammetric processing and provide practical suggestions about their optimal arrangement:

- The availability of a large number of images, deriving from several surveys, did not appear to be a sufficient condition for obtaining optimal results in terms of MAPE[%];

- The image scale parameter was the parameter that had the greatest influence on tree reconstruction from point clouds, as already reported in previous studies (Marzulli et al., 2020) with an optimal parameter value equal to 1/2;

- Point density parameter should be set to Optimal or Low, according surveys are inside or outside/inside;

- The average point cloud density (points/m^3) values relating to the point clouds considered optimal (Table 4) were between approximately 17,388 and 28578. Point clouds with lower or higher average point

Table 12
Average MAPE[%] errors for each point Cloud associated to the diameter computations.

MAPE[%]	DX130	DY130	DX200	DY200	DX400	DY400
Cloud1	5.04	4.56	4.04	4.52	6.86	5.74
Cloud2	4.13	3.58	4.55	4.98	7.58	6.86
Cloud3	5.53	5.21	4.47	4.85	6.25	8.40
Cloud4	**15.96**	**16.56**	**15.37**	**13.47**	**31.97**	**17.17**
Cloud5	4.57	5.54	5.23	4.92	6.24	6.31
Cloud6	11.19	8.43	11.73	9.59	11.14	13.66
Cloud7	5.66	4.14	5.56	5.73	5.68	7.31
Cloud8	**34.35**	**42.33**	**28.49**	**31.30**	**33.33**	**26.06**
Cloud9	5.40	4.70	4.91	4.10	8.74	5.50
Cloud10	6.09	3.85	5.31	5.45	9.30	5.42
Cloud11	5.27	4.35	4.65	4.91	8.42	6.59
Cloud12	13.78	11.96	10.50	12.52	22.39	13.92
Cloud13	5.60	4.58	5.54	4.00	6.29	7.54
Cloud14	7.49	4.07	6.05	5.70	9.11	4.80
Cloud15	5.80	4.65	4.54	4.55	7.27	6.38
Cloud16	**24.48**	**22.24**	**27.13**	**19.98**	**22.02**	**17.99**

Table 13
Average MAPE[%] errors for each point Cloud associated to the circumference reconstructions.

MAPE[%]	CircX130	CircX200	CircX400
Cloud1	3.88	3.37	3.25
Cloud2	2.46	2.86	3.25
Cloud3	2.42	3.08	4.62
Cloud4	12.41	10.19	19.88
Cloud5	3.02	2.38	1.90
Cloud6	7.00	8.99	8.22
Cloud7	4.69	5.11	5.55
Cloud8	**33.98**	**20.23**	**29.02**
Cloud9	4.69	4.85	4.78
Cloud10	3.67	3.94	3.71
Cloud11	2.98	2.36	2.67
Cloud12	10.06	9.57	14.72
Cloud13	4.03	4.61	2.08
Cloud14	3.61	3.48	2.38
Cloud15	2.28	2.47	3.45
Cloud16	**18.21**	**19.51**	**18.50**

Table 14
Pix4D Mapper software parameters for the point clouds elaboration.

Point cloud	Flight	Captured images	Calibrated images	Image Scale	Point Density
1	Outside	849	759	1/2	Optimal
5	**Outside**	**557**	**487**	**1/2**	**Optimal**
9	Outside/ Inside	1262	1150	1/2	Optimal
10	Outside/ Inside	1262	1150	1/4	Optimal
11	**Outside/ Inside**	**1262**	**1150**	**1/2**	**Low**
13	Outside/ Inside	754	668	1/2	Optimal
15	**Outside/ Inside**	**754**	**668**	**1/2**	**Low**

cloud density values than the considered range did not reach optimal results;

- Tables 9 and 10 show it is possible, by averaging the MAPE [%], to establish the optimal point clouds and indicate the strategies to obtain them. The first strategy starts from a relatively low number of images compensated by an optimal densification during point processing; the second reduces the densification and compensates information loss with a greater number of images, obtained by combining several surveys (Table 3). In summary, the main features of the best point clouds are reported in Table 15a and 15b.

Table 16 reports the results derived from a collection of papers, whose contributions can be classified into three main categories: (i) the plot type; (ii) the size of the study area and (iii) the RMSE value associated with the DBH.

By comparing the accuracy results with those of the work of Piermattei et al. (2019) referring to a study area of dimensions identical to those of the present study, we observed that the RMSE values associated with the DBH assessment outperformed those of Piermattei (0.88 cm vs. 4.02 cm). In the work of Liu et al. (2018) on a plot smaller than the one considered in the present study, the DBH measurements reached a higher accuracy level but slightly poorer than those gained in the present study (0.92 to 1.13 vs. 0.88). Finally, in the work of Mokroš et al. (2018), in a slightly larger plot, the DBH measurement had an accuracy of 1.80 cm, greater than the 0.88 cm obtained in the present study.

In addition to the analysis of the state-of-the-art of passive sensing under forest canopy, it is worth noting some studies that focus on the use of active sensing in drones in boreal forests (Hyyppä et al., 2020; Hyyppä et al., 2021). The proposed methodologies rely on the utilization of a laser scanner system mounted to the bottom of big UAV. This differentiates from the methodology presented in this article, which utilizes small-sized drones with a camera for passive sensing and a processing procedure based on Structure from Motion (SFM) algorithms.

6. Conclusions

The main current technological development line for forestry monitoring considers the use of TLS systems in the context of qualitative/quantitative surveys. These systems are characterized by high levels of accuracy and transportability, which are well suited to forest contexts. Nevertheless, the implementation of these techniques requires highly skilled technicians, proficient in both the data acquisition phase and the subsequent processing phase. Additionally, the considerable costs associated with hardware and software components must also be taken into account.

In the present study, a new operational paradigm was introduced that consisted of the use of UAV under the canopy cover and not above it, as outlined in many scientific publications. This approach has a series of technical/operational advantages represented initially by the reduction of technological costs and by the greater simplicity of data acquisition and processing: for example, the possibility of overcoming obstacles (undergrowth and landed trees) by remotely managing the UAV flight.

In the present study, terrestrial photogrammetry in the forest was carried out to develop efficient drone acquisition schemes and optimize the software parameters for the treatment of the collected data (quantity of images to be processed, processing times, and accuracy of the final results). The continuous updates of the algorithms underlying SfM photogrammetry, as well as the ever-increasing efficiency of photographic sensors mounted on drones, will contribute to increasing the accuracy of the proposed approach in the near future, both in terms of data acquisition and in processing.

The results obtained from the experimental setup were found to be comparable, and in some cases even superior, to those achieved by state-of-the-art terrestrial photogrammetry systems, as evidenced by a thorough comparison with authoritative literature.

The future prospects of this novel approach show great promise, particularly in the realm of periodic monitoring activities in forest areas. It is worth noting that the maintenance and replacement costs associated with unmanned aerial vehicles (UAVs) are entirely negligible when contrasted with the expenses incurred by using terrestrial laser scanning (TLS) technologies.

In our perspective, the proposed approach would be most beneficial for various stakeholders involved in forest resource management, including regional bodies, forest companies, national parks, and managers responsible for protected areas. These actors play critical roles in the monitoring and decision-making processes aimed at safeguarding

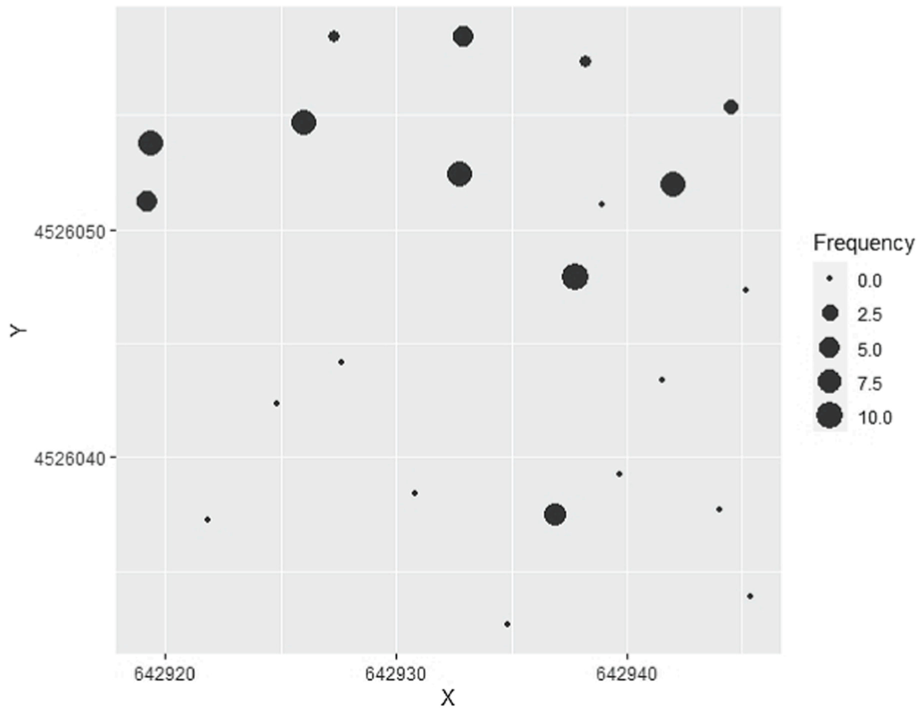

Fig. 9. Better reconstructed trees within the sample.

Table 15a
Main parameters of data acquisition.

Point cloud	Survey	Number of surveys	Setting	Captured images	Total data collection time [min:sec]
5	Outside	2	2, 3	557	21:51
11	Outside/ Inside	5	1, 2, 3/ 1, 3	1262	48:54
15	Outside/ Inside	3	2, 3/3	754	29:47

Table 15b
Main parameters of data processing.

Point cloud	Calibrated images	Image Scale	Point Density	Average Point cloud Density [points/m^3]	Processing time (point cloud densification) [h:min]
5	487	1/2	Optimal	28.578	1:17
11	1150	1/2	Low	17.388	2:29
15	668	1/2	Low	17.502	1:05

Table 16
Comparison between the present study and the literature.

Study	Plot type	Size	RMSE [cm]
Piermattei et al. (2019)	circular circular circular squared	Diameter 30 m diameter 40 m diameter 40 m 30 m × 30 m	4.02
Liu et al, 2018	squared	20 m × 20 m	From 0.92 to 1.13
Mokroš et al., (2018)	squared	35 m × 35 m	1.80
Liang et al., 2015	squared	30 m × 30 m	2.38

forest resources.

Regarding the potential limitations of the proposed methodology, primary considerations revolve around its applicability to diverse forest types characterized by varying tree densities and the presence of a dense understory, which may impede the efficacy of drone surveys. Future developments and field experimentations will deepen those aspects.

To conclude, the proposed methodology can be successfully applied not only for a one-time survey of a forest but also for recurring measurements in a sustainable manner. The cost-effectiveness of the equipment, field personnel, and survey duration makes it a suitable tool for assessing the ecological condition of a forest with relatively minimal effort.

Declaration of Competing Interest

The authors declare that they have no known competing financial interests or personal relationships that could have appeared to influence the work reported in this paper.

Data availability

Data will be made available on request.

Acknowledgements

The present study has been funded by the following projects:

1. “Studio sperimentale della pianificazione assestamentale avanzata relativa ai complessi forestali di proprietà della Regione Puglia” managed and funded by A.R.I.F. Apulia Region (Regional Agency for Irrigation and Forestry activities of the Apulia Region).
2. “Metodi innovativi per la stima del volume legnoso ritraibile dai tagli boschivi in Puglia” managed and funded by Regione Puglia - Sezione Gestione Sostenibile e Tutela delle Risorse Forestali e Naturali. Dipartimento Agricoltura, Sviluppo Rurale e Ambientale Dipartimento di Scienze Agro-Ambientali e Territoriali dell’Università degli Studi di Bari Aldo Moro (DiSAAT)

References

Barca, E., Porcu, E., Bruno, D., Passarella, G., 2017. An automated decision support system for aided assessment of variogram models. Environ. Model. Softw. 87, 72–83.

Brede, B., Calders, K., Lau, A., Raumonen, P., Bartholomeus, H.M., Herold, M., Kooistra, L., 2019. Non-destructive tree volume estimation through quantitative structure modelling: comparing UAV laser scanning with terrestrial lidar. Remote Sens. Environ. 233, 111355 https://doi.org/10.1016/j.rse.2019.111355.

Brede, B., Terryn, L., Barbier, N., Ms, B.H., Bartolo, R., Calders, K., Derroire, G., Krishna Moorthy, S., Lau, A., Levick, S.R., Raumonen, P., VerbeeckH, W.D., Whiteside, T., van der Zee, J., Herold, M., 2022. Non-destructive estimation of individual tree biomass: allometric models, terrestrial and UAV laser scanning. Remote Sens. Environ. 280, 113180.

Calders, K., Adams, J., Armston, J., Bartholomeus, H., Bauwens, S., Bentley, L.P., Chave, J., Danson, F.M., Demol, M., Disney, M., Gaulton, R., Moothy, S.M.K., Levick, S.R., Saarinen, N., Schaaf, C., Stovall, A., Terryn, L., Wilkes, P., Verbeeck, H., 2020. Terrestrial laser scanning in forest ecology: expanding the horizon. Remote Sens. Environ. 251, 112102.

Chai, T., Draxler, R.R., 2014. Root mean square error (RMSE) or mean absolute error (MAE)?–Arguments against avoiding RMSE in the literature. Geosci. Model Dev. 7 (3), 1247–1250.

Dandois, J.P., Ellis, E.C., 2010. Remote sensing of vegetation structure using computer vision. Remote Sens. (Basel) 2 (4), 1157–1176.

Dandois, J.P., Ellis, E.C., 2013. High spatial resolution three-dimensional mapping of vegetation spectral dynamics using Computer Vision. Remote Sens. Environ. 136, 259–276.

De Croon, G., De Wagter, C., 2018. Challenges of autonomous flight in indoor environments. In: In 2018 IEEE/RSJ International Conference on Intelligent Robots and Systems (IROS). IEEE, pp. 1003–1009.

Dwyer, R.A., 1987. A faster divide-and-conquer algorithm for constructing Delaunay triangulations. Algorithmica 2 (1), 137–151.

Fredman, M.L., Tarjan, R.E., 1987. Fibonacci heaps and their uses in improved network optimization algorithms. Journal of the ACM (JACM) 34 (3), 596–615.

Gao, Y., Skutsch, M., Paneque-Gálvez, J., Ghilardi, A., 2020. Remote sensing of forest degradation: a review. Environ. Res. Lett. 15 (10), 103001.

Holopainen, M., Talvitie, M., 2012. Forest inventory by means of tree-wise 3D-measurements of laser scanning data and digital aerial photographs. Int Arch. Photogramm. Remote Sens. Spat. Inf. Sci 36, 67–72.

Hyyppä, E., Hyyppä, J., Hakala, T., Kukko, A., Wulder, M.A., White, J.C., Kaartinen, H., 2020. Under-canopy UAV laser scanning for accurate forest field measurements. ISPRS J. Photogramm. Remote Sens. 164, 41–60.

Hyyppä, J., Yu, X., Hakala, T., Kaartinen, H., Kukko, A., Hyyti, H., Hyyppä, E., 2021. Under-canopy UAV laser scanning providing canopy height and stem volume accurately. Forests 12 (7), 856.

Iglhaut, J., Cabo, C., Puliti, S., Piermattei, L., O'Connor, J., Rosette, J., 2019. Structure from motion photogrammetry in forestry: a review. Current Forestry Reports 5 (3), 155–168.

Küng, O., Strecha, C., Beyeler, A., Zufferey, J.C., Floreano, D., Fua, P., Gervaix, F., 2011. The accuracy of automatic photogrammetric techniques on ultra-light UAV imagery. Int. Arch. Photogramm. Remote Sens. Spatial Inf. Sci. XXXVIII-1/C22, 125–130.

Lawrence, K.D., Klimberg, R.K., 2016. Vol. 11 of Advances in business and management forecasting. Bingley, Emerald Group of Publishing, UK.

Liang, X., Jaakkola, A., Wang, Y., Hyyppä, J., Honkavaara, E., Liu, J., Kaartinen, H., 2014. The use of a hand-held camera for individual tree 3D mapping in forest sample plots. Remote Sens. (Basel) 6 (7), 6587–6603.

Liang, X., Wang, Y., Jaakkola, A., Kukko, A., Kaartinen, H., Hyyppä, J., Honkavaara, E., Liu, J., 2015. Forest data collection using terrestrial image-based point clouds from a handheld camera compared to terrestrial and personal laser scanning. IEEE Trans. Geosci. Remote Sens. 53 (9), 5117–5132.

Liang, X., Kankare, V., Hyyppa, J., Wang, Y., Kukko, A., Haggren, H., Yu, X., Kaartinen, H., Jaakkola, A., Guan, F., Holopainen, M., Vastaranta, M., 2016. Terrestrial laser scanning in forest inventories. ISPRS J. Photogramm. Remote Sens. 115, 63–77.

Liu, J., Feng, Z., Yang, L., Mannan, A., Khan, T.U., Zhao, Z., Cheng, Z., 2018. Extraction of sample plot parameters from 3D point cloud reconstruction based on combined RTK and CCD continuous photography. Remote Sens. (Basel) 10 (8), 1299.

Luoma, V., Saarinen, N., Wulder, A., White, J.C., Vastaranta, M., Holopainen, M., Hyyppa, J., 2017. Assessing precision in conventional field measurements of individual tree attributes. Forests 8 (2), 38.

Marzulli, M.I., Raumonen, P., Greco, R., Persia, M., Tartarino, P., 2020. Estimating tree stem diameters and volume from smartphone photogrammetric point clouds. Forestry: An Int. J. Forest Res. 93 (3), 411–429.

McRoberts, R.E., Tomppo, E.O., 2007. Remote sensing support for national forest inventories. Remote Sens. Environ. 110 (4), 412–419.

Micheletti, Natan; Chandler, Jim; Lane, Stuart N. (2015): Structure from motion (SFM) photogrammetry. Loughborough University. Journal contribution. https://hdl.handle.net/2134/17493.

Mokroš, M., Liang, X., Surový, P., Valent, P., Čerňava, J., Chudý, F., Tunak, D., Salon, S., Merganič, J., 2018. Evaluation of close-range photogrammetry image collection methods for estimating tree diameters. ISPRS Int. J. Geo Inf. 7 (3), 93.

Ozkan, U.Y., Demirel, T., 2018. Estimation of forest stand parameters by using the spectral and textural features derived from digital aerial images. Appl. Ecol. Environ. Res. 16 (3), 3043–3060.

Piermattei, L., Karel, W., Wang, D., Wieser, M., Mokroš, M., Surový, P., Kore, M., Tomaštík, J., Pfeifer, N., Hollaus, M., 2019. Terrestrial structure from motion photogrammetry for deriving forest inventory data. Remote Sens. (Basel) 11, 950.

Puliti, S., Ørka, H.O., Gobakken, T., Næsset, E., 2015. Inventory of small forest areas using an unmanned aerial system. Remote Sens. (Basel) 7 (8), 9632–9654.

Raumonen, P., Casella, E., Calders, K., Murphy, S., Åkerblom, M., Kaasalainen, M., 2015. Massive-scale tree modelling from TLS data. ISPRS Ann. Photogramm. Remote Sens. Spat Inf. Sci 2 (3), 189.

Tmušić, G., Manfreda, S., Aasen, H., James, M.R., Gonçalves, G., Ben-Dor, E., Brook, A., Polinova, M., Arranz, J.J., Meszaros, J., Zhuang, R., Johansen, K., Malbeteau, Y., Pedroso de Lima, I., Davids, C., Herban, S., McCabe, M.F., 2020. Current practices in UAV-based environmental monitoring. Remote Sens. (Basel) 12 (6), 1001.

Ullman, S., 1979. The interpretation of structure from motion. Proc. R. Soc. Lond. B 203 (1153), 405–426.

Westoby, M.J., Brasington, J., Glasser, N.F., Hambrey, M.J., Reynolds, J.M., 2012. 'Structure-from-Motion'photogrammetry: a low-cost, effective tool for geoscience applications. Geomorphology 179, 300–314.

White, J.C., Coops, N.C., Wulder, M.A., Vastaranta, M., Hilker, T., Tompalski, P., 2016. Remote sensing technologies for enhancing forest inventories: a review. Can. J. Remote. Sens. 42 (5), 619–641.